Extraction, representation and interpretation of nanoscale domain structure information from small–angle scattering patterns

N. Stribeck

Institute TMC, University of Hamburg, Bundesstr. 45, D–20146 Hamburg, Germany
Norbert.Stribeck@desy.de

ABSTRACT

A method for SAXS analysis and its applications to the field of materials science is presented and corresponding papers are reviewed. The method permits to extract and visualize topological structure information contained in scattering patterns from small-angle scattering (SAS) without complex pretreatment. Multi-dimensional data can be processed. Such data are for instance accumulated in the field of materials science in time–resolved in–situ SAXS experiments with synchrotron radiation. The result is a multi-dimensional chord distribution function (CDF), that is defined as the Laplacian of the correlation function. It is equivalent to the autocorrelation of the gradient of the electron density. The procedure is, in particular, adapted to the analysis of the nanoscale structure of samples with fiber symmetry, such as of polymer fibers or of strained elastomers. Multi-dimensional relations among morphological components become apparent in real space and help to elucidate the nature of processes governing evolution of nanostructure. The background subtraction problem is proposed to be solved by spatial frequency filtering. According to the proposed notion, the domain structure information of the studied nanocomposite is contained in the spatial frequency band between background and noise. The method can be applied to scattering curves from isotropic samples as well. In this case chord length distributions (CLD) or interface distributions (IDF) are computed. Here the advantage of the method is the possibility to automate data evaluation and thus to become able to process large data sets that are frequently recorded in time resolved experiments. Examples from straining and melting studies of thermoplastic elastomers and polyethylene are presented.

Key words: Small–angle scattering, synchrotron radiation, polymers, nanostructure, materials properties, crystallization

1 Introduction

The extraction of structural data from small–angle scattering (SAS) patterns has been a problem of constant interest to researchers for many years, particularly in the field of bulk polymer materials where such images frequently are related to a non–ideal multi–phase structure made from domains. Investigation of this domain structure, its evolution and its relation to materials properties is considered a main issue of materials science. In the mid–nineties dedicated synchrotron radiation sources became available [1, 2]. Scattering patterns from oriented polymer materials recorded with two–dimensional detectors revealed a wealth of well–resolved features and posed a new challenge, namely to develop adequate methods of data analysis. An early idea was simplification of the problem by extracting curves that reflect partial aspects of the domain structure [3–10]. In this case established methods for the analysis of small–angle X–ray scattering (SAXS) curves can be applied to correct for the deviations from an ideal multi–phase structure [11–17]. Fluctuation of the electron density inside the phases, for instance, causes a slowly varying background in the scattering data [11]. The decay of the scattering intensity resulting from Porod's law [18] is increased by a smooth transition zone at the phase boundary [11], and roughness added to the boundary itself is raising the specific surface [13]. All these slowly varying effects are superimposed in the scattering pattern. From curves they can be separated after resorting to extensive assumptions, but whenever anisotropic scattering patterns are to be analyzed, the related ambiguities become even more elusive. Moreover, the extraction of curves turns out to be of limited value only. The curves extracted from high–quality patterns frequently turn out to be too complex to be fitted by the common and simple models of domain shape and arrangement.

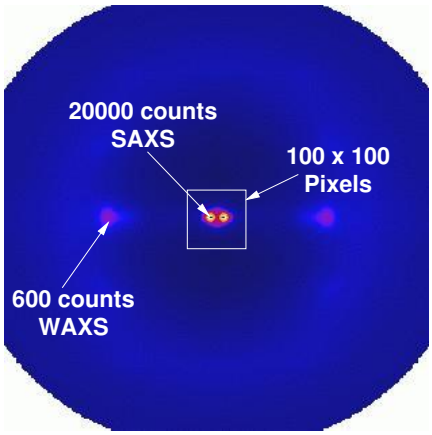

Figure 1: Demonstration of a high–quality 2D scattering pattern. SAXS and WAXS from drag line spider silk accumulated during 30 s at the ESRF (Courtesy of Chr. Riekel).

Thus the analytical method has to preserve the multi–dimensionality found in the scattering patterns. The first problem then is the elimination of the multi–dimensional background related to the non–ideal nature of the real nanostructure. Taking advantage of the observation that all the discussed backgrounds are slowly varying functions, this elimination is carried out by spatial filtering of the recorded scattering pattern: The relevant information on multi–phase nanostructure is said to show up in the spatial frequency band between the slowly varying backgrounds related to the non–ideal nature on one side, and to the statistical noise of the measurement on the other. Finally a representation of the nanostructure information is proposed, that is adapted to human perception because it is defined in such a way that it exhibits a multi–dimensional image of the domains and their mutual arrangement in real space. As long as it is not necessary to introduce an orientation distribution, the nanostructure can be interpreted directly. But if the structure must be deconvoluted from an orientation distribution, the ideas of Murthy [19, 20] may help to solve the problem.

Already published applications of the reviewed method [21, 22] to polymer processing [23–26] show its potential to elucidate both the structure–processing and the structure–properties relationships that are sought for in the field of materials science.

2 The method and its modules

2.1 Advance of synchrotron scattering technique

During the past two decades the scattering technique available at synchrotron radiation sources has advanced considerably. In 1982 a typical synchrotron radiation run at HASYLAB in Hamburg did not exceed 30 min and the beam position jumped frequently. Today the radiation run lasts 16 h and the beam position is stable. Twenty years ago the injected current was not higher than 30 mA. Today it is 160 mA. With the well–focusing optics installed during the past five years, high quality scattering patterns can be accumulated during a moderate period of time.

Figure 1 shows the small–angle X–ray scattering (SAXS) and the wide–angle X–ray scattering (WAXS) of drag line spider silk recorded simultaneously at the European Synchrotron Radiation Facility (ESRF) in 30 s on a CCD detector. At beam line A2 of HASYLAB in Hamburg the SAXS of a good scatterer (SBS block copolymer) is recorded with similar S/N–ratio and in similar time, but 10fold spatial resolution on a “MarCCD 185” detector. Using such apparatus polymer materials can be investigated aiming at quantitative nanostructure analysis during processing, mechanical or thermal load.

SAXS images from rotating anode laboratory sources are not competitive. In order to achieve the S/N–ratios required for a quantitative analysis a polymer sample has to be exposed for several hours.

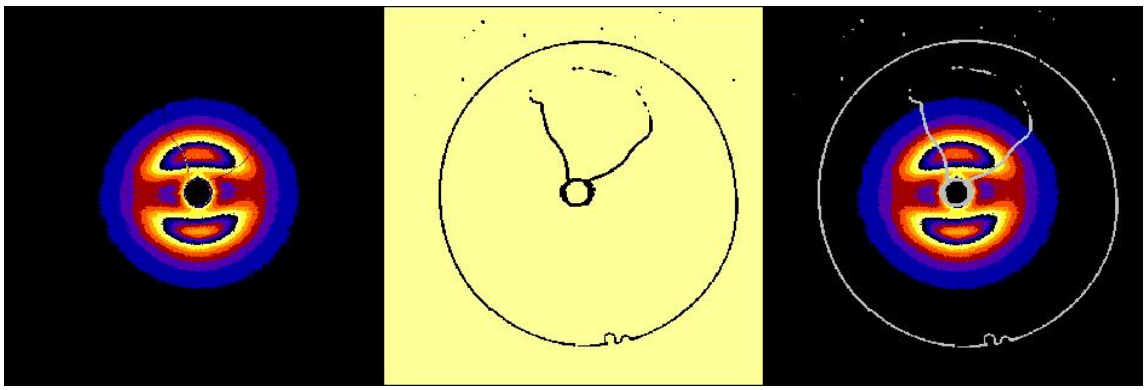

Figure 2: A complex image flaw (shades of wires holding the "pin diode beam stop") can be corrected by Sobel–filtering. From left to right: Original pattern. Wire mask. Distorted pixels set to zero.

2.2 Digital image processing

Although even isotropic scattering data benefit from the advance of technique, the information content on the nanostructure remains relatively low. Anisotropic samples, on the other hand, may exhibit a wealth of distinct peaks and other features in the corresponding scattering patterns. Fiber patterns, in particular, are well–suited for the demonstration of advanced data analysis for two reasons. Firstly, polymer materials with fiber symmetry are ubiquitous in technical applications; secondly, the total information content of their SAXS is contained in a single two–dimensional (2D) scattering pattern.

2D scattering data, in general, are subject to some distortions, and the initial reason to utilize digital image processing tools results from the need to mark blind spots and flaws in the image. A challenging example is shown in Figure 2. Here the pixels of the image are distorted by the half–shade of wires running through the path of the scattered radiation. The distorted pixels have been marked by application of a Sobel filter. In successive steps all the pixels that are invalid due to various reasons must be marked. Then the image is centered and aligned with respect to its principal axis. Finally many of the invalid pixels can be filled from symmetry considerations, and the remaining white patches may be filled by two–dimensional extrapolation based on radial basis functions [27]. As a result the pixel matrix is filled with smooth valid data.

After this image–oriented treatment, and after sample absorption and machine background has been operated, the business of scattering pattern evaluation can be started.

2.3 Chord distribution with fiber symmetry

2.3.1 General definitions

Let $I(\mathbf{s})$ be the observed SAS intensity. The magnitude of the scattering vector be defined by $|\mathbf{s}| = (2/\lambda)\sin\theta$, with λ the wavelength of radiation and 2θ the scattering angle. Common notations will be used for both the case of isotropic scattering patterns by writing $I(\mathbf{s}) = I(s)$ with $s = |\mathbf{s}|$, and for the case of a scattering pattern with fiber symmetry, $I(\mathbf{s}) = I(s_{12}, s_3)$ with $s_{12} = \sqrt{s_1^2 + s_2^2}$ and the direction of s_3 defining the symmetry axis of the pattern.

2.3.2 Intensity projection onto a plane

If the scattering pattern is already complete in a subspace of the 3D reciprocal space, the suitable projection [3, 4, 6, 28] has to be carried out before the following 1D or 2D Fourier transformation. In classical methods special Fourier kernels are employed, that are implicitly comprising the projection. But for the data evaluation of scattering "images" with fiber symmetry it is convenient to utilize commercial standard software for image processing like *pv–wave* [29], and to carry out the necessary

projection

$$I_P(s_1, s_3) := \{I(s_{12}, s_3)\}(s_1, s_3) = \int I(s_{12}, s_3)\, ds_2, \tag{1}$$

the 2D Fourier transformation $\mathscr{F}^2(I_P)(r_{12}, r_3) := P(r_{12}, r_3)$ of which is known as the 2D (electron–) density correlation function [30] in cylindrical co–ordinates.

2.3.3 A generalized chord distribution

In the case of isotropic data the features of the nanostructure can be visualized more clearly in a chord length distribution (CLD) [31] or in an interface distribution (IDF) [32] than in a correlation function. Now the question arises, how the one–dimensional concepts of the CLD and the IDF can be generalized for the case of multi–dimensional scattering data from multi–phase systems. The complete treatment has been published elsewhere [21]. A brief overview is presented here.

The autocorrelation of the gradient of the density distribution $\rho(\mathbf{r})$ can be defined as a chord distribution $z(\mathbf{r}) = (\nabla\rho(\mathbf{r}))^{*2}$ for any multi–dimensional case. It is equivalent to the Laplacian $\Delta P(\mathbf{r})$ of the correlation function $P(\mathbf{r})$ and can be computed from the multi–dimensional Fourier transformation of the scattering intensity $I(\mathbf{s})$ multiplied by $4\pi^2 s^2$. For samples with fiber symmetry we start from the projected intensity I_P and obtain

$$I_L(s_1, s_3) = 4\pi^2 s^2\, I_P(s_1, s_3) \tag{2}$$

with $s^2 = \sqrt{s_1^2 + s_3^2}$ in this context. It has been proven convenient now to subtract a constant, in order to suppress the otherwise strong increase of intensity for large s in $I_L(s_1, s_3)$. This subtraction helps to avoid a damping of the observed oscillations in the pattern when the next evaluation step is applied.

In the next evaluation step the non–ideal character of the studied multiphase structure has to be considered. In the classical methods [11, 32, 33] this is accomplished by subtraction of several slowly varying backgrounds (density fluctuations, width of the phase transition, domain roughness). These backgrounds are well justified from physical reason, but difficult to separate. Result of this operation is an interference function, $G(\mathbf{s})$, that shall become subject to a Fourier transformation. Since our interest is not the study of the non–ideal character, but to gain information on shape and arrangement of the nanometer size domains, the composite slowly–varying background in the SAS image is considered a parasitic effect. Under this premise a suitable background can be extracted from the SAXS pattern itself by computing the low–pass filtered pattern, $f_{\ell,r_c}(I_L(\mathbf{s}))$. Its subtraction reduces the central singularity in the Fourier transformation of $I_L(\mathbf{s})$. Hence an adapted interference function $G(\mathbf{s})$

$$G(\mathbf{s}) = I_L(\mathbf{s}) - f_{\ell,r_c}(I_L(\mathbf{s})) \tag{3}$$

is defined based on a low–pass filter operator $f_{\ell,r_c}()$ with a cut–off frequency r_c. On one hand, a background correction based on a low–pass filter is not more arbitrary than the background fitting methods commonly employed in evaluation of small–angle scattering curves. On the other hand, the definition of the low–pass filter is valid for deliberate dimensionality of the recorded data. A variation of filter parameters shows that the anticipated chord distribution function (CDF) is altered marginally only, as long as a filter with smooth frequency response is chosen and the cutoff frequency is kept low. For the common Butterworth filter this means that a low order has to be chosen in order not to imprint artifacts resulting from discontinuities of the filter response function. A first–order Butterworth filter

$$f_{\ell,r_c}(I_L(\mathbf{s})) = \mathscr{F}^{-1}\left(\mathscr{F}(I_L(\mathbf{s}))(\mathbf{r})\, \frac{1}{(1 + r/r_c)^2}\right) \tag{4}$$

($r = |\mathbf{r}|$. Here $\mathscr{F}()$ designates the multi–dimensional Fourier transformation) has proved feasible in many fields of research. Application shows that the cutoff frequency r_c can be varied within a fairly wide range without change of the apparent topological parameters. Nevertheless, after background subtraction there remain intensity discontinuities at the circumference of the sensitive area of the detector. The general procedure to minimize the corresponding artificial undulations in real space is multiplication by an appropriate windowing function ("Hann window") [34].

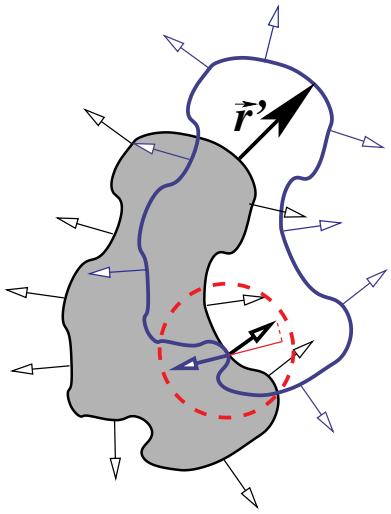

Figure 3: Particle–ghost autocorrelation of gradient vectors generates the multi–dimensional chord distribution. Its positive and negative values are a function of relative surface orientation.

Finally the interference function $G(\mathbf{s})$ is subject to a discrete Fourier transformation. The result

$$z(\mathbf{r}) = -\mathscr{F}(G(\mathbf{s})) \tag{5}$$

is the chord distribution function (CDF) $z(\mathbf{r})$. Thus the complete morphological information concerning size and arrangement of domains is right at hand in the physical space function $z(r_{12}, r_3)$ after few evaluation steps.

In the case of fiber symmetry, $z(\mathbf{r})$ can be depicted by a surface in space which shows positive and negative peaks with respect to the (r_{12}, r_3)–plane. It can be interpreted employing Porod's "particle–ghost" notion [35–38] after minor modification (Figure 3). Whereas the value of the correlation function $\gamma(\mathbf{r})$ as a function of ghost displacement $\mathbf{r}'$ is determined by the volume shared by particle and ghost, the value of the CDF $z(\mathbf{r})$ is given by the scalar product of the gradient vectors. Obviously there are only contributions at those positions where surfaces of particle and ghost are shared. Moreover, the value of $z(\mathbf{r})$ is not only a function of the number of interacting surface elements, but also a function of their orientation. Surfaces crossing at right angles do not contribute. Definitions of chord length distributions (CLD) avoid this dependence from surface orientation, but are difficult to generate in the multidimensional case. Parallel and antiparallel gradient vectors generate function values of different sign. The sign of $z(\mathbf{r})$ is chosen to let autocorrelation of antiparallel gradient vectors generate a positive contribution to $z(\mathbf{r})$. For example, the highlighted pair of gradient vectors in Figure 3 will contribute almost the maximal positive value. It is obvious that ghost–displacement in an ensemble of particles with convex shape will not start to generate negative contributions to $z(\mathbf{r})$ before ghosts start to overlay alien particles. Thus the corresponding negative contributions can be considered a generalization of translational repeat, whereas positive contributions are related to domain (and "intermitted domain") sizes. The first mentioned are generalizations of a lattice property, whereas the latter are related to the domain shapes and distributions of the multi–phase structure.

2.4 Isotropic data, spatial frequency filtering and interface distributions

Background elimination by spatial frequency filtering can be applied to isotropic scattering data as well, as has been demonstrated in a previous publication [22]. This method is, in particular, advantageous when aiming at an automatization of data evaluation. Automatization is becoming an important issue both as the volume of data to be analyzed is bulging because of an increasing number of time–resolved experiments, and as the background–sensitive interface distribution function (IDF) analysis is gaining importance [6, 12, 23, 39–54].

Let us define an estimated constant background, c_{Fl}, by minimizing the function

$$T_c(c_{Fl}, A_p) = \sum_k \left(s_k^4 (I_k - c_{Fl}) - A_P\right)^2, \tag{6}$$

with the sum being extended over all measured points in the region where Porod's law is estimated to be valid. In a second step

$$I_{Pl}(s) = s^4 (I(s) - c_{Fl}) \tag{7}$$

is computed, which ends in an almost horizontal asymptote, if Porod's region was reasonably chosen. Now let us define a low–pass filter operator, $f_{\ell,x_c}()$ with a cut–off frequency x_c defined in real space. As in the anisotropic case, a first–order Butterworth filter

$$f_{\ell,x_c}(I_{Pl}(s)) = \mathscr{F}^{-1}\left(\mathscr{F}(I_{Pl}(s))(x)\ \frac{1}{(1+x/x_c)^2}\right) \tag{8}$$

is chosen. After subtraction of the low pass filtered background

$$G_1(s) = I_{Pl}(s) - f_{\ell,x_c}(I_{Pl}(s)) \tag{9}$$

the interference function is obtained. A Hann window is applied in the isotropic case, too. Finally the interference function is subject to a 1D Fourier transformation yielding the IDF $g_1(x)$.

It shall be pointed out that in the case of considerable domain surface roughness, i.e. whenever the integral $\int G_1(s)\ ds$ becomes strongly negative, the background elimination may be carried out repeatedly, until the postulation $\int G_1(s)\ ds \approx 0$ is fulfilled. If such iterated interference functions are analyzed, it should be carefully checked, if the substantial aspects of the nanostructure have passed the applied cascade of spatial frequency filters.

3 Examples of CDF method application

3.1 SIS thermoplastic elastomers studied during straining

The complete study reviewed here has been published elsewhere [55].

Material. Commercial SIS triblock copolymer CAROM TLI 30 (CAROM S.A., Oneşti, Romania) with a total molecular mass of $M_w = 105\,\mathrm{kg/mol}$ was investigated. Molecular mass of the polyisoprene middle block is $M_w = 73.5\,\mathrm{kg/mol}$. According to IR spectroscopy the polyisoprene block contains 88.9% 1,4–*cis* units, 2.1% 1,4–*trans* units and 9.0% 3,4*(vinyl)* units. Neat material (sample designation: SIS) and a brominated sample (designation: SISbr) were studied.

Scattering experiments. Ultra small–angle X-ray scattering (USAXS) was performed in the synchrotron beam line BW4 at HASYLAB, Hamburg, Germany. USAXS images were collected by a two–dimensional position sensitive Gabriel detector (512×512 pixels of $0.4\times0.4\,\mathrm{mm}^2$). The sample–to–detector distance was set to 12870 mm. Samples with marks were mounted in a straining stage positioned in the synchrotron beam, slowly strained up to the desired elongation and exposed for 30 min. Images were corrected for flat detector response and blind areas were masked. Background subtraction and sample absorption were subsequently operated. Center and fiber axis of the pattern were determined. Images were aligned and averaged with respect to the four quadrants resulting in peak maximum counts of at least 10000 (Sample SIS at highest elongation). To cover a wider angular range, small–angle X-ray scattering measurements were carried out at HASYLAB, beam line A2 using image plate exposed for 60 s.

Results. Examining three–dimensional (3D) plots of the scattering intensity (Figure 4) it becomes obvious that the complex shape of the scattering pattern cannot be explained in terms of common simple notions on nanostructure.

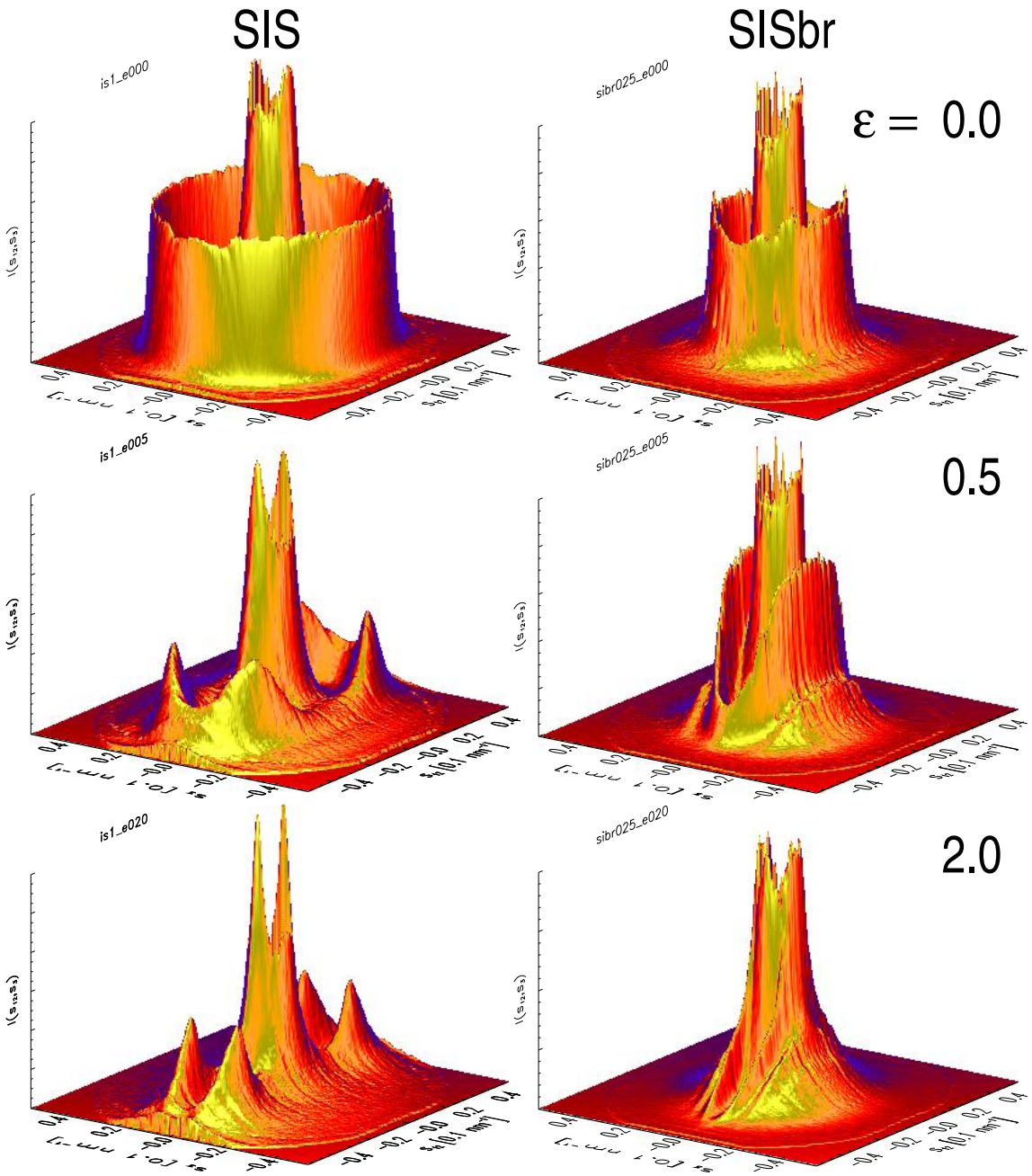

Figure 4: USAXS intensity as a function of elongation for neat (SIS) and brominated (SISbr) triblock copolymer.

Nanostructure representation in physical space. Multidimensional chord distributions $z(\mathbf{r})$ have been computed from the scattering patterns according to the method described in section 2.3. Views of $z(\mathbf{r})$ from the top (Figure 5) and from the bottom (6) exhibit shape and arrangement of the polystyrene domains in the polyisoprene matrix. Domains are best recognized in the view from the top. Long periods result in negative peaks and are visible when viewed from the bottom of the CDF.

At zero elongation, SIS shows many pronounced correlations among domains on a macro lattice with a long period of $L_e = 27\,\mathrm{nm}$. SISbr, on the other hand, exhibits a fast decay of the correlations on a lattice with a long period $L_e = 47\,\mathrm{nm}$. Comparison shows that long periods determined both from the scattering pattern and the CDF by simple graphical method are close to each other. As a function of increasing elongation the central domain expands in meridional direction and a pronounced central "watch–shaped" region is formed for both samples. This region contains the information on the autocorrelation of both the polystyrene domains and the polyisoprene matrix material. It is surrounded by peaks describing the correlation among different domains. In between deep "long period valleys" are extending in meridional direction. The SIS sample, in particular, shows a very high degree of order which shall be discussed in the sequel.

But before the contours at high elongation will be used to extract some quantitative information, the general nanostructural model shall be distinguished from 3D plots of the chord distribution presented in Figure 5 and Figure 6. Based on the "particle–ghost–displacement" notion the peaks from the CDF can be attributed to nanostructural features. In the 3D representations of Figure 5 characteristic peaks are labeled. A cylinder ("Cy") gives strong peaks whenever the flat caps of particle and ghost touch at the meridian. An ellipsoid ("El") gives a strong ring close to the center. Increased intensity of this ring at the meridian can be explained by flattened caps of the ellipsoidal particles. A microfibrillar ("mf") nanostructure is revealed by a pair of additional strong peaks on the meridian. Its maxima are found at the most probable length of the elastic gap between two polystyrene domains. An outward shoulder reveals the dimension of a composite particle made from two neighboring polystyrene ellipsoids with one gap length in between. Such structure is not observed in the CDF from sample SIS. Instead, four small peaks surrounding the center indicate the shortest correlated displacement between neighboring cylinder caps in a macro lattice. Figure 6 is a bottom view of the CDF. It reveals the long period distributions of the nanostructure as a function of elongation and position in (r_{12}, r_3)–plane. SIS at high elongation shows a well–separated arrangement of individual peaks, which is typical for any lattice. Decay of the peaks as a function of their distance from the center demonstrates loss of order (short–range order). SISbr long periods are organized differently. They are concentrated close to the meridional axis and form more or less continuous walls even at high elongation.

While for one–dimensional structures suitable model functions are at hand [25, 56] which describe and link long period distributions and particle size distributions, the observed variety of multidimensional peaks reveals the challenge related to the task of fitting a model to the multidimensional CDF. Interpretation of these rich functions, on the other hand, may add to the understanding of nanostructure in polymer materials.

Nanostructure extraction. After that the fundamental properties of the nanostructure have been deduced from 3D plots, contour plots (Figure 7 and Figure 8) can be utilized to gain a quantitative description of the average structure from peak maxima positions in $z(\mathbf{r})$. Obviously the result is an approximation, because shape and overlap of particle correlation peaks are not considered. The left side of Figure 7 presents CDF contour plots of the sample SIS at high elongation ($\varepsilon = 2.0$). The top plot shows the positive peaks, the bottom plot the negative peaks with labels. From the position of the strongest peaks on the meridian, (d), a domain height of approx. 50 nm is determined. From the width of this peak in lateral dimension a cylinder diameter of 8 nm is estimated. The arrangement of the polystyrene cylinders in the polybutadiene matrix can is extracted from the positions of the other observable peaks. These data result in a model of the nanostructure, which is sketched on the right side of Figure 7. Peak (a) at a position (r_{12}, r_3) equal to $(12\,\mathrm{nm}, 14\,\mathrm{nm})$: reveals the displacement from a cylinder cap to the closest cap of a neighboring cylinder. (b), $(38\,\mathrm{nm}, 50\,\mathrm{nm})$: from cylinder top cap to the bottom cap of the closest neighbor in lateral direction. (c): $(114\,\mathrm{nm}, 18\,\mathrm{nm})$: from top cap to the bottom cap of a cylinder displaced both in lateral and in longitudinal direction. (d) has been explained. The peak from top cap to closest neighbor top cap (x) is a long period. An intermitted particle is the correlation (e): $(0\,\mathrm{nm}, 50\,\mathrm{nm})$ between the left side of a cylinder and the right side of its neighbor to the right. The observed misplacement may result from asymmetric shape of the particle size distributions. A different explanation would resort to a second component to the nanostructure with cylinders oriented parallel to the equator [57, 58]. The two possibilities should be distinguishable by model fit.

The closest long period in lateral direction (x): $(35\,\mathrm{nm}, 0\,\mathrm{nm})$ as already mentioned. A second order in lateral direction (x'): $(70\,\mathrm{nm}, 0\,\mathrm{nm})$ is seen for every long period. The other long periods are found at (y): $(18\,\mathrm{nm}, 52\,\mathrm{nm})$; (y'): $(52\,\mathrm{nm}, 52\,\mathrm{nm})$;

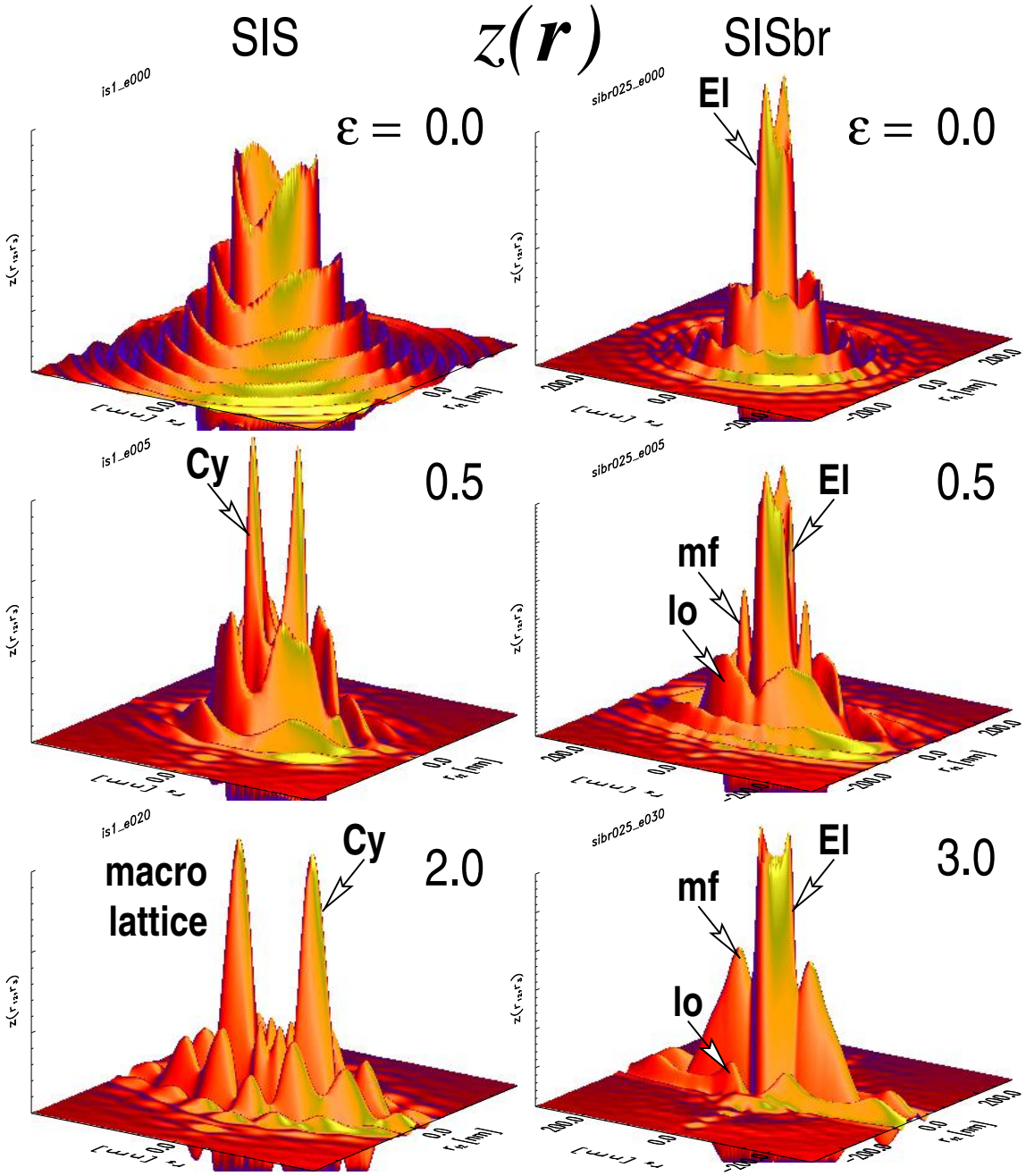

Figure 5: 3D top view ("*domain face*") $z(\mathbf{r})$ of the CDF as a function of elongation for neat (SIS) and brominated (SISbr) triblock copolymer. "El" marks peaks from an ellipsoidal particle. "Cy" points at cylinder peaks. "mf" indicates microfibril peaks on the meridian and "lo" shows lateral order by domain–domain correlations.

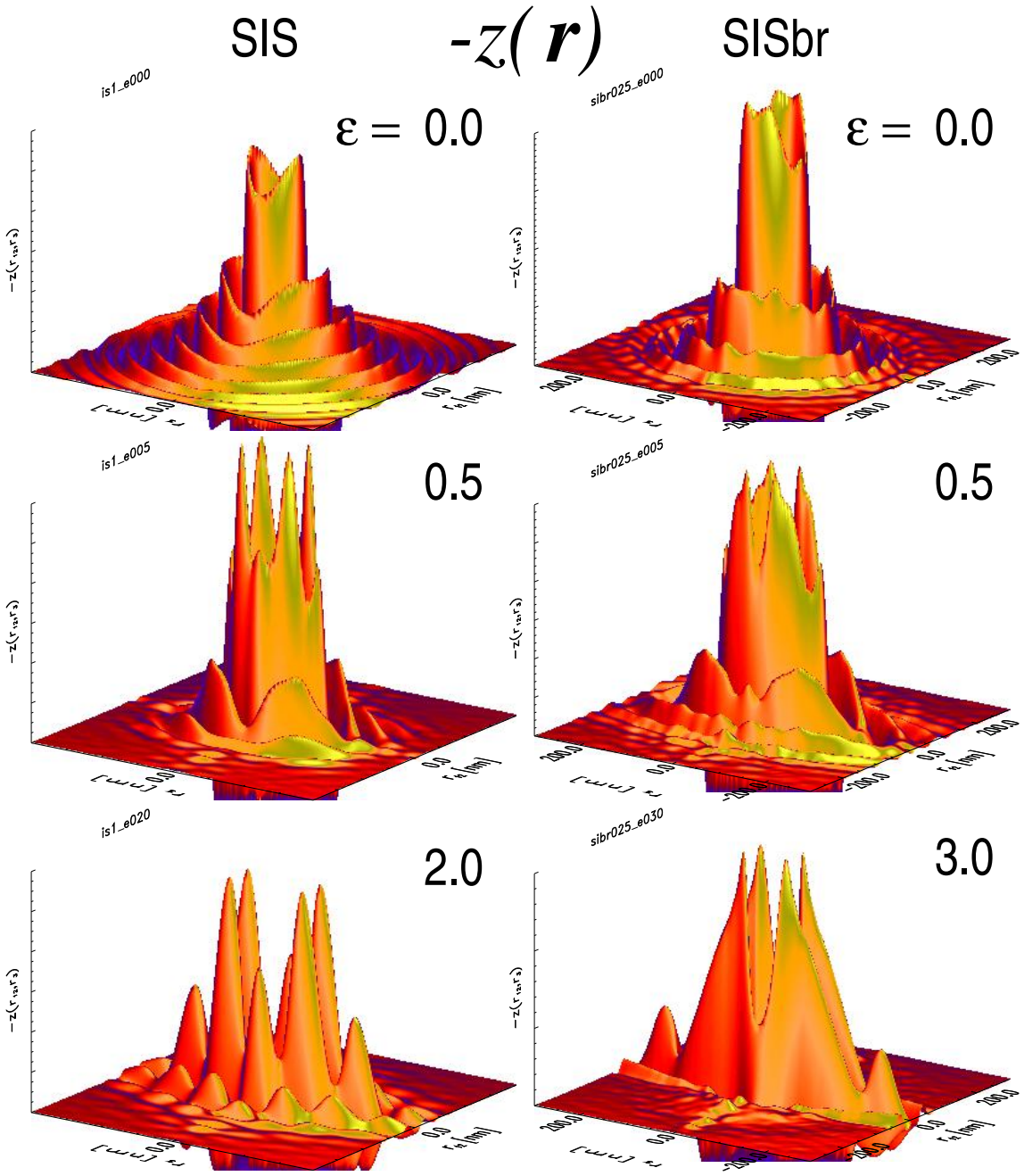

Figure 6: 3D bottom view ("*lattice face*") $-z\left(\mathbf{r}\right)$ of the chord distribution as a function of elongation for neat (SIS) and brominated (SISbr) triblock copolymer. Peaks showing up here are long periods.

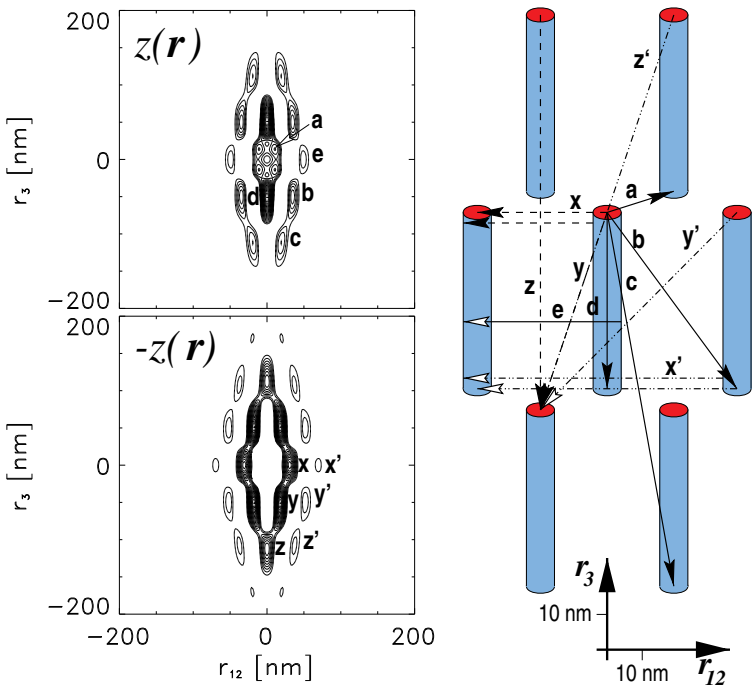

Figure 7: **Left:** CDF contour plots of sample SIS at elongation $\varepsilon = 2.0$. Domain face (top) and lattice face (bottom). Peak labels correspond to labeling in a sketch of the corresponding nanostructure (**right**).

(z): $(0\,\mathrm{nm}, 114\,\mathrm{nm})$, and (z'): $(35\,\mathrm{nm}, 114\,\mathrm{nm})$. Thus all the observed strong peaks in the CDF can be explained by a hexagonal arrangement of elongated cylinders with next–neighbor correlations only.

For the sample SISbr the corresponding set of labeled contour plots and a model sketch are presented in Figure 8. From the main axes of the central ellipsoidal ring an average polystyrene domain diameter of $(a) = 24\,\mathrm{nm}$ and a height of $(b) = 38\,\mathrm{nm}$ is determined. The ellipsoidal shape of the fundamental particle causes more pronounced peak smearing from shape than in the case of the cylinders discussed above. But moreover, the arrangement of samples inside the SISbr sample appears to be less perfect. The observed domain peaks are found at $c \approx (c_1 + c_2)/2 \approx 86\,\mathrm{nm}$; $d \approx (45\,\mathrm{nm}, 62\,\mathrm{nm})$; $e \approx (27\,\mathrm{nm}, 182\,\mathrm{nm})$. Here strong second orders of long periods are not observed. The highest long period peaks are found under oblique displacement $x \approx (28\,\mathrm{nm}, 44\,\mathrm{nm})$. The second strong long period correlation is at the meridian $y \approx (0\,\mathrm{nm}, 182\,\mathrm{nm})$. Everywhere on a closed path around the origin long periods are found. Only the weak second orders are found on isolated islands.

Here CDF analysis reveals that, indeed, the sample is characterized by a microfibrillar structure with correlations among particles along the meridian. Additionally the CDF shows considerable correlations among ellipsoids under oblique angle, which are not extracted by conventional SAXS analysis. Some other distinct features of the CDF, in particular the wall–shaped long periods in the (r_{12}, r_3)–plane, may lead to novel insight into fundamentals of such nanostructures.

3.2 Melting of oriented, high–pressure injection molded PE

High–pressure injection molded rods from poly(ethylene) (Lupolen 6021 D, BASF) exhibit a core–shell structure. In order to achieve high orientation, an equilibrated cool melt of 160°C was injected into a cold mold. The pressure–time diagram of the molding process is shown in Figure 9. Maximum mold pressure was 444 MPa and final mold pressure 336 MPa after 180 s. Three more samples with different molding pressure were studied. The lowest maximum mold pressure was 412 MPa. In DSC all samples exhibit bimodal melting with peak maxima at 131°C and 141°C. Samples for the USAXS investigation were sectioned from the shell and the core of the rod, respectively, using a low–speed diamond saw.

Ultra small–angle X–ray scattering (USAXS) was performed in the synchrotron beam line BW4 at HASYLAB, Hamburg, Germany. USAXS images were collected by a two–dimensional position sensitive Gabriel detector (512×512 pixels of $0.4 \times 0.4\,\mathrm{mm}^2$). The sample–to–detector distance was set to 12690 mm.

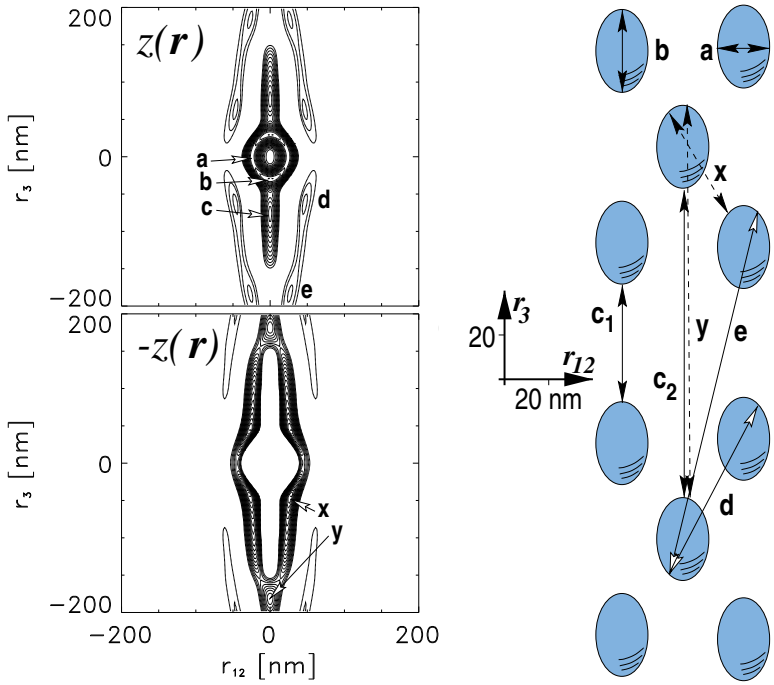

Figure 8: **Left:** CDF contour plots of sample SISbr at elongation $\varepsilon = 2.0$. Domain face (top) and lattice face (bottom). Peak labels correspond to labeling in a sketch of the corresponding nanostructure (**right**).

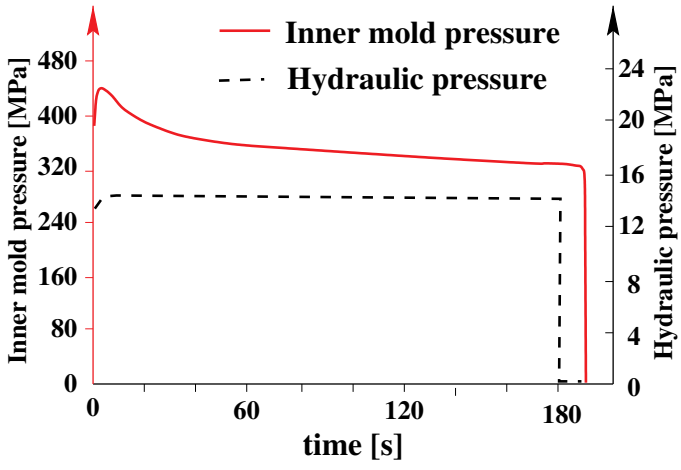

Figure 9: Pressure–time diagram of the injection molding process.

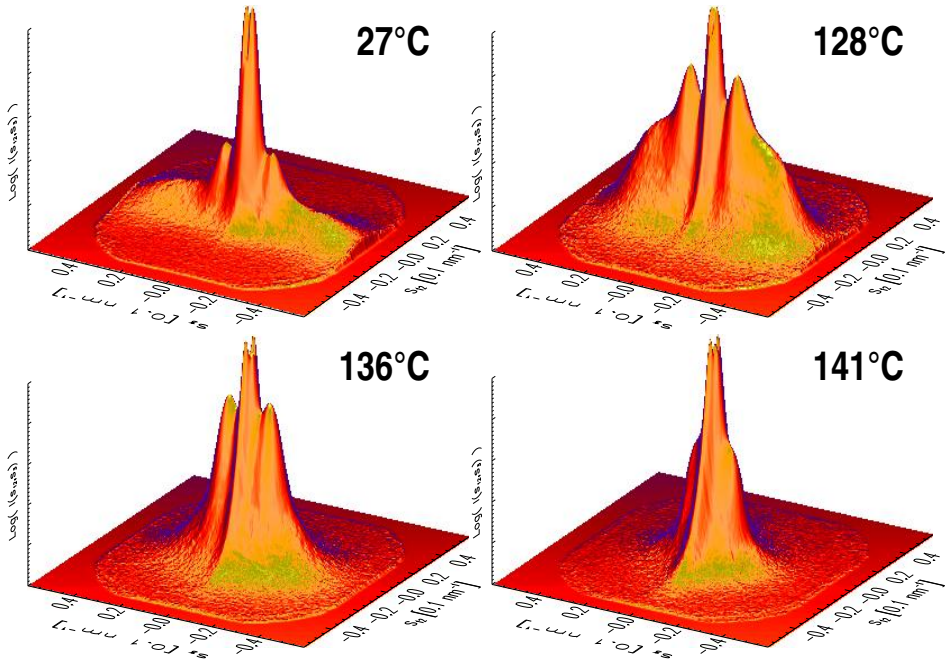

Figure 10: USAXS intensity $\log\left(I\left(\mathbf{s}\right)\right)$ from the shell zone of a PE rod at various temperatures during heating.

During image collection, each sample was heated from 25°C to 150°C. Below 100°C a heating rate of 5°C/min was chosen. Thereafter the heating rate was slowed to 2°C/min. Images were accumulated for 90 s. Data storing took 30 s. The complete study is published elsewhere [59].

The USAXS patterns. Figure 10 exhibits the USAXS intensity from the shell zone of the highest pressure molded PE rod at specific temperatures during heating of the sample. Data are normalized to primary intensity and machine background is subtracted.

Sharp long period reflections with a peak maximum corresponding to 100 nm are obvious in all patterns. The peaks are placed on top of an intensity ridge extending along the meridian. As a function of increasing temperature the shape of the ridge is changing, whereas the peak appears to be almost unchanged. The ridge disappears before melting. Early at 128°C equatorial scattering is indicated. With increasing temperature it becomes more pronounced and vanishes last when melting.

A direct interpretation of these patterns appears to be difficult and ambiguous. In unpublished work we have tried to analyze the intensity projected on to the meridian quantitatively [6] utilizing the method of interface distribution analysis [32, 56]. None of the scattering curve could be fitted by a simple model of lamellae or lamellar stacks, respectively.

3D–Chord distributions of the shell material. Figure 11 shows 3D chord distribution functions $z\left(\mathbf{r}\right)$ of the shell material at various temperatures during heating. All plots are show the same interval in all three directions.

Obviously a lamellar system is present at ambient temperature. Each of the strong, triangle shaped peaks describes both crystalline lamellae and amorphous ones. The corresponding layer thickness distributions are broad and cause the corresponding peaks merge into one. The long period (26 nm) is much smaller than expected from the peak maximum of the scattering pattern.

At 128°C peak heights have grown caused from different thermal expansion of crystalline and amorphous phases, respectively. From the width of the triangles an average lateral extension of 70 nm is determined. The undulation frequency in front of the strong peaks has halved just as the temperature of 128°C has been reached. Thus the long period now has doubled. In the center of the lower peaks of second order an indentation is observed, which is still unexplained at this temperature.

At 136°C the first minimum in the CDF in meridional direction (i.e. the long period) is found at 95 nm. The imperfect layers have melted and the only observable feature is the layer stack corresponding to the strong peaks in the scattering pattern. Again,

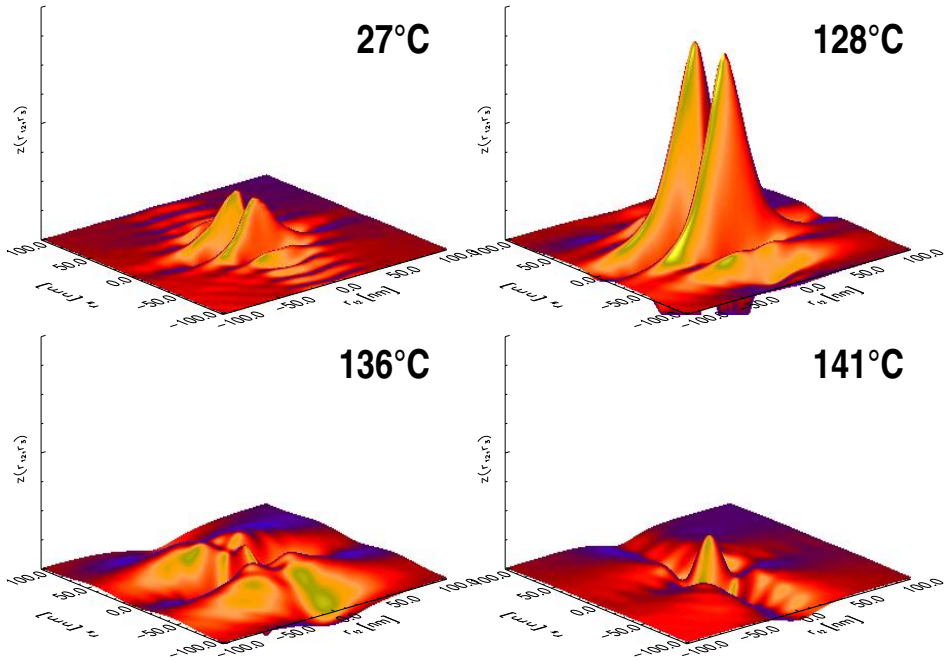

Figure 11: Shell zone of the PE rod: 3D chord–distributions with fiber symmetry, $z\,(\mathbf{r})$ as a function of temperature during heating in the range $r_{12}, r_3 \in (-100\,\mathrm{nm}, 100\,\mathrm{nm})$.

the distribution of layer thicknesses is very broad. The indentation from the last pattern has increased to form a trough extending along the meridian.

At 141^{o}C the trough has engraved itself to from a deep valley on the meridian. A more shallow, modulated valley is extending along the equator of the CDF. Single lamellae with a very broad distribution are indicated by the low hills in the pattern.

Minima in the valleys are associated to long periods [21]. Figure 12 shows the contours of the long periods as a function of temperature. It is observed that the long period doubles first at 128^{o}C and a second time at 136^{o}C. But still the long equatorial streak indicates the autocorrelation of a lamellar system. At 141^{o}C the nanostructure has changed fundamentally. The streak at the equator has shrunk and indicates the predominance of domains which are narrow in lateral direction ("blocks"). On the meridian a row of crystal nuclei is observed that form a distorted one–dimensional lattice with a long period of 95 nm. The arrow points at the first order of the lattice. The superimposed weak modulation is continued over the whole area of the (r_{12}, r_3)–plane and is an artefact (caused from the remnant small step at the edge of the sensitive plane of the detector). At the equator the main modulation is somewhat stronger and appears to be out of phase what the base plane modulation is concerned. If we agree to attach some importance to this observation, it is supporting the notion of Strobl [48, 50, 52, 60] according to which crystalline lamellae are generated from a planar arrangement of blocks.

Based on these observation it appears to be justified to assume, to a first approximation, that during heating first those crystallites are melting, which were formed last during crystallization. So let us imagine to revert time and to discuss the observed process in terms of a crystallization. Doing so permits to proceed from the simple to the complex nanostructure. Under this premise the results reveal that upon the start of crystallization tiny nuclei are forming row structures along fiber direction. From these nuclei lamellae are growing in lateral direction. The thicknesses of these lamellae are not uniform (20 nm to 60 nm). During the course of cooling new and thin crystal layers are generated somewhere in between the primary lamellae. When the material is cooled even further, the long period is halved a second time. All the time the most regular period remains constant and given by the average distance of the nuclei in the rows which after all causes the point–shaped long period reflections in the scattering pattern. The subdivision of the primary long period in the subsequent insertion crystallization is highly irregular and generates the intensity ridge extending along the meridian. The strength of the equatorial streak is correlated with the strength of the row structure. Thus the CDF analysis reveals that for the studied materials the insertion model of crystallization [61, 62] is more probable than the two–stack model [63]. While the scattering pattern is emphasizing the harmonic components of the structure, the CDF shows all the regular and irregular components with equal weight and the complexity of the nanostructure is revealed.

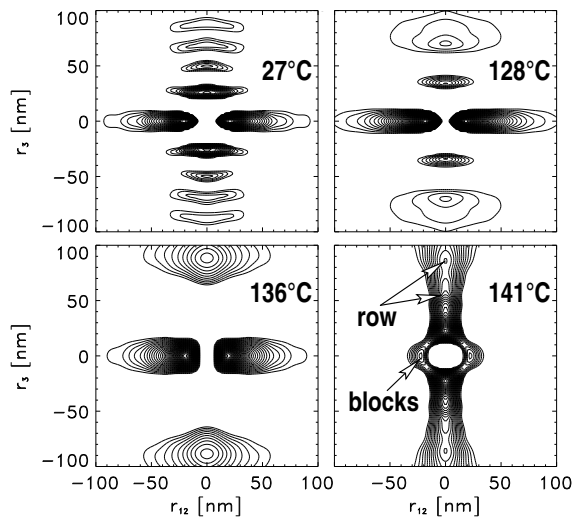

Figure 12: Shell zone of the PE rod: 3D chord–distributions with fiber symmetry, $-z\left(\mathbf{r}\right)$ as a function of temperature during heating in the range $r_{12}, r_3 \in (-100\,\mathrm{nm}, 100\,\mathrm{nm})$.

The core structure is discussed in the original paper [59].

3.3 Nanostructure of isotropic, injection molded UHMWPE

In this investigation isotropic materials were studied in a time–resolved experiment during melting and recrystallization. More than 500 scattering patterns were recorded and analyzed utilizing the automated spatial frequency filtering method for isotropic data followed by a quantitative IDF analysis based on the model of lamellar stacking. The full paper is published elsewhere [25].

Experimental. 3 grades of ultra high molecular weight polyethylene (UHMWPE, Hoechst–Celanese Inc.) of different molecular mass were investigated ($M_w/\left(10^6\ \mathrm{g/mol}\right) = 4, 5, 6$). From the supplied powders rods were injection molded at 3 different pressures ($p = 210$, 240, 280 MPa). The materials were equilibrated in the molten state (252^{o}C) for 5 min and then pressurized for 30 minutes. Thereafter the rods were recovered by cooling the samples at a rate about 1^{o}C/min under an isobaric condition.

Ultra small angle X-ray scattering (USAXS) was performed in the synchrotron beam line BW4 at HASYLAB, Hamburg, Germany under similar conditions as mentioned above. During image collection, each sample was heated from 25^{o}C to 250^{o}C with 5^{o}C/min. Images were accumulated for 90 s. Data storing took 30 s. So there is one image per 10^{o}C. Samples M6H and M4M (for sample denominations cf. Figure 13) were additionally heated with 6^{o}C/min up to 115^{o}C, slowed to 2^{o}C/min during the melting up to 145^{o}C, speeded up to 6^{o}C/min again up to 250^{o}C. Thus here images were collected every 4^{o}C in the most interesting temperature range. DSC scans were carried out in a Perkin–Elmer DSC–7 in a range from 25^{o}C to 180^{o}C with a heating rate of 5^{o}C/min.

DSC results. DSC thermograms are shown in Figure 13. Characteristic parameters and sample designations used in the sequel are indicated in the figure. The samples exhibit two melting peaks. As a function of increasing molding pressure the low–temperature peak is decreasing, whereas the high–temperature peak becomes stronger. This finding is commonly explained by "extended chain lamellae" formation by high–pressure crystallization, as was first reviewed by Wunderlich [64]. According to the DSC thermograms samples prepared at $280\,\mathrm{GPa}$ exhibit almost total conversion to extended chain lamellae which melt at temperature above 140^{o}C.

Results. Scattering patterns as a function of molecular weight, molding pressure and sample temperature are shown in Figure 14. Interface distribution functions (IDF), $g_1\left(x\right)$ [32], were extracted from the scattering patterns as is described in section 2.4. Considering an ideal two–phase system the IDF represents the probability distribution of finding two interfaces

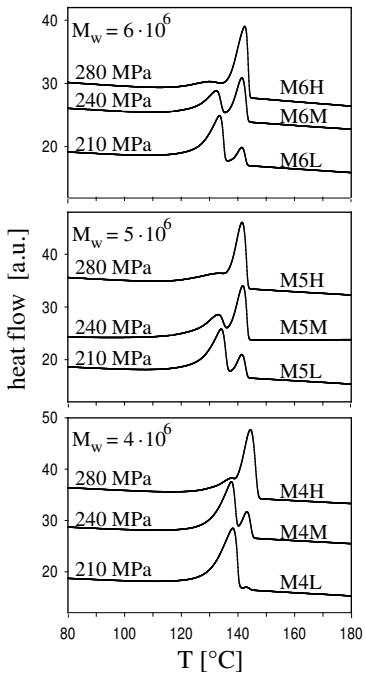

Figure 13: Melting of UHMWPE as a function of molecular mass and molding pressure studied by differential scanning calorimetry (DSC). Varied parameters are indicated on the left of each curve, sample denominations on the right.

(between a crystalline layer and the adjacent amorphous region) at a distance x from each other. The IDF is proportional to the second derivative of the one–dimensional correlation function, $\gamma_1(x)$ [65].

Several models were tested to fit the IDF data. As indicated by the complex shape of the scattering curves, a single stack proved insufficient. Thus a second component had to be added. In order to obtain perfect fits it turned out to be sufficient to assume that the second component comprises an ensemble of isolated lamellae with a Gaussian thickness distribution (cf. Figure 15).

Close to melting pure particle scattering was observed with some of the samples.

Figure 14 shows the scattering data in a representation emphasizing the scattering features of a domain structure built from lamellae. A bimodal character of the nanostructure is most clearly observed at high pressure and high molecular weight, where the scattering of an ensemble of thick lamellae is obvious in the vicinity of $s = 0$. In all sub-figures the s–axis extends from left to right and comprises an interval $0\,\mathrm{nm}^{-1} < s < 0.055\,\mathrm{nm}^{-1}$. The temperature axis extends from front to back and runs from 20°C to 160°C.

Interface distributions during UHMWPE heating as a function of of molecular mass and molding pressure are shown in Figure 16. At the upper bound of the x–axis (110 nm) almost all correlations among layers are faded away. During heating from room temperature to 100°C the dominant effect is a collective increase of all peak heights. It is caused from the different thermal expansion coefficients of the amorphous and the crystalline domains [66].

Figure 17 shows some of the structural parameters as a function of temperature, molding pressure, and molecular mass. Intervals of confidence as determined by the curve fitting algorithm are indicated by error bars.

Solid lines are related to the lamellar stack component. The curves without symbol marks show the weight. The weight shows an almost linear increase up to a temperature of 100°C. At higher temperature weight decreases due to melting of the crystalline domains.

Filled squares show the average thickness of crystalline layers from the stack, $\bar{t}_{c,s}$. They can be identified from the fact that the relative widths of their distributions are considerably narrower than the relative widths of the amorphous layers. Moreover, at high temperature the amorphous distributions become very wide indicating transformation from stacks to uncorrelated crystalline lamellae. The average thickness of the crystalline lamellae is close to 20 nm. It is independent of molecular weight and molding pressure for all samples up to a temperature of 120°C.

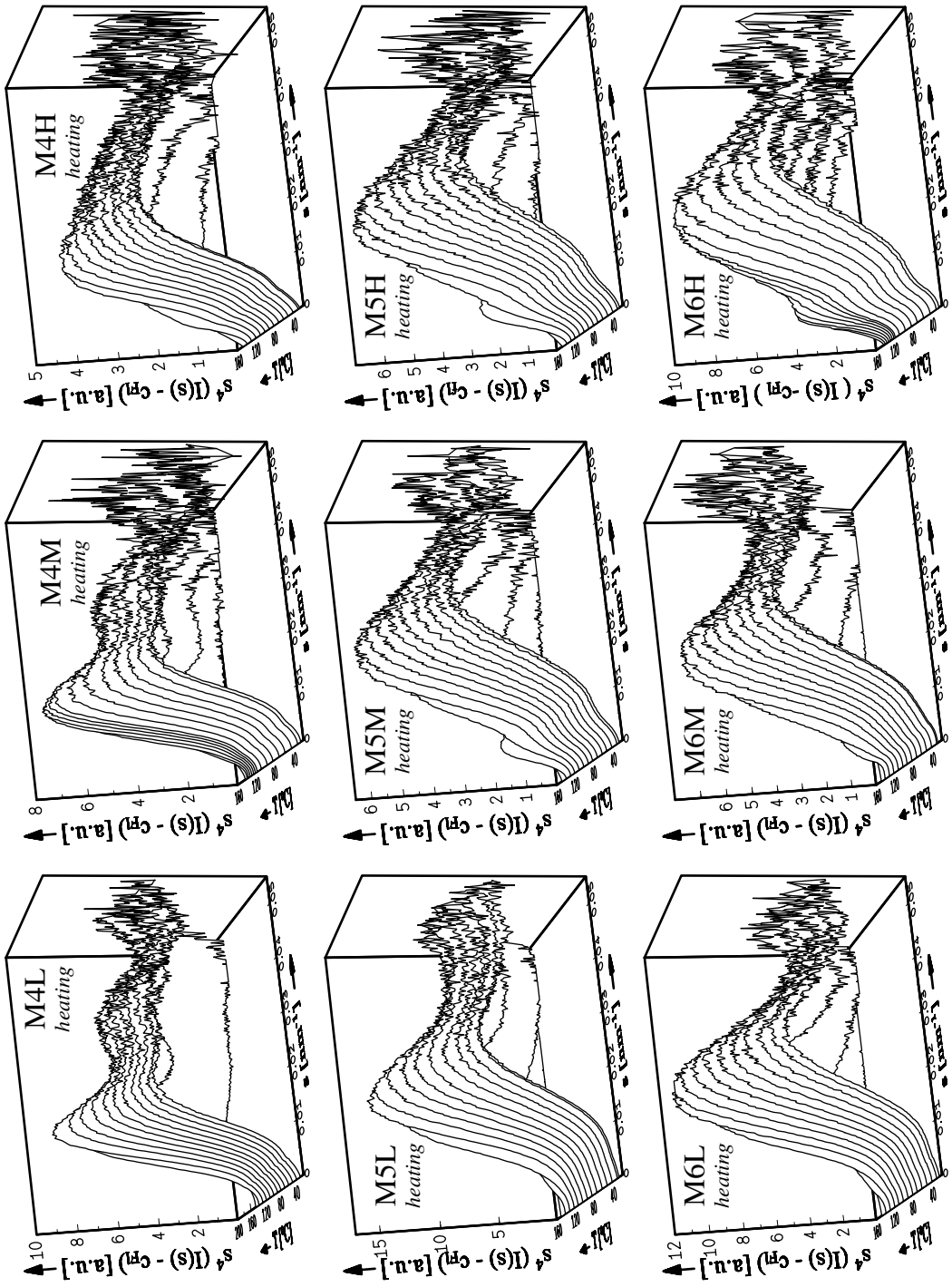

Figure 14: Melting of UHMWPE as a function of molecular mass and molding pressure. USAXS curves $s^4\left(I\left(s-c_{Fl}\right)\right)$ with c_{Fl} estimated from the tail of the curve.

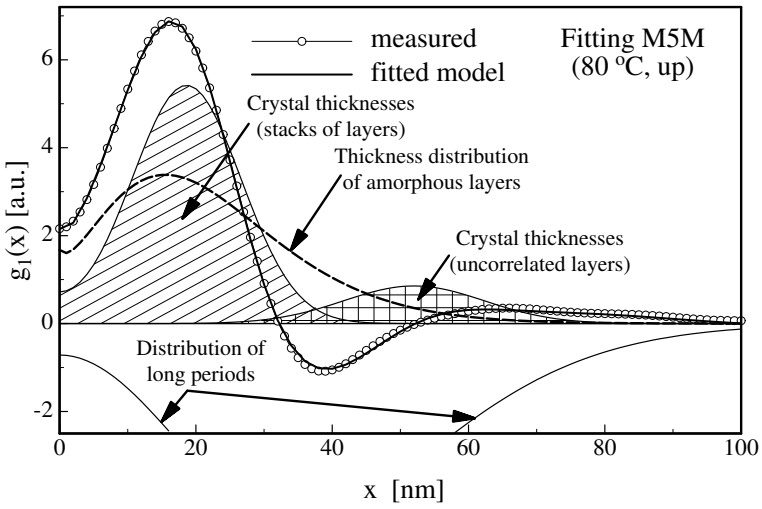

Figure 15: Demonstration of IDF fit by a model comprising an ensemble of uncorrelated crystalline lamellae (cross–hatched layer thickness distribution) and stacked lamellae (hatched: crystal thickness distribution, dashed: amorphous thicknesses, below x–axis: number distribution of long periods).

Table 1: Volume fraction $V_{p,c}$ of uncorrelated crystalline lamellae with respect to the total volume of the crystalline phase as a function of molding pressure and molecular mass of UHMWPE.

	$p = 210$ MPa	240 MPa	280 MPa
$M_w = 4\,10^6$g/mole	0.37	0.31	0.42
$M_w = 5\,10^6$g/mole	0.23	0.36	0.43
$M_w = 6\,10^6$g/mole	0.28	0.31	0.46

Average amorphous layer thicknesses, $\overline{t}_{a,s}$, are marked by open squares. Up to a temperature of 100°C they are almost constant. As a function of increasing pressure a considerable increase of $\overline{t}_a$ is observed for all samples independent of molecular weight. Linear crystallinity $v_{c,\ell} = \overline{t}_{c,s} / (\overline{t}_{c,s} + \overline{t}_{a,s})$ is smallest for the grade M4 with the lowest molecular mass (0.41 at low pressure, 0.30 at high pressure). The two grades M5 and M6 start with $v_{c,\ell} = 0.5$ at low pressure and end with 0.44 at high pressure. Thus crystallinity depression inside the stacks as a function of molding pressure is smaller for the grades M5 and M6.

The average layer thickness of the uncorrelated crystalline particles, $\overline{t}_{c,p}$, are shown by dashed curves marked with filled circles. Here the high molecular mass grades M5 and M6 are similar again. $\overline{t}_{c,p}$ remains constant up to 120°C. It is 25 nm for low molding pressure and 50 nm for both medium and high molding pressure. Grade M4 is different. For low and medium molding pressure we observe $\overline{t}_{c,p} = 40\,\mathrm{nm}$ over a wide temperature range. The sample prepared at high molding pressure shows a linear decrease of $\overline{t}_{c,p}$ starting with 80 nm at room temperature and ending with 40 nm at 100°C. As compared to the M5 and M6 grade, the layer thickness distributions are very wide, indicating imperfection. Even more imperfection can be concluded from the rapid joint collapse of both components in M4L at high temperature, observed in their weight curves. This is reflected in the feature of a single DSC melting peak of M4L (Figure 13).

Let us now discuss the effect of high molding pressure on the formation of thick crystalline lamellae, which is frequently addressed as "formation of extended chain lamellae" [64, 67–72]. Table 1 shows the volume fraction $V_{p,c}$ of uncorrelated, thick lamellar particles with respect to the total volume occupied by the crystalline phase at 30°C. The high molecular weight grades M5 and M6 exhibit the frequently reported increase of the fraction of thick, uncorrelated lamellae as a function of increasing pressure. Again, the results of grade M4 can be explained by its imperfect nanostructure.

Figure 18 presents the variation of the crystalline volume, $x\,h_c\,(x)$, as a function of crystalline layer thickness x, temperature, molecular mass, and molding pressure. For low pressure (left column) the two populations of crystal layer thicknesses cannot be separated visually in the plots of M5L and M6L. Nevertheless, both DSC and quantitative SAXS data evaluation suggest that two populations should be present.

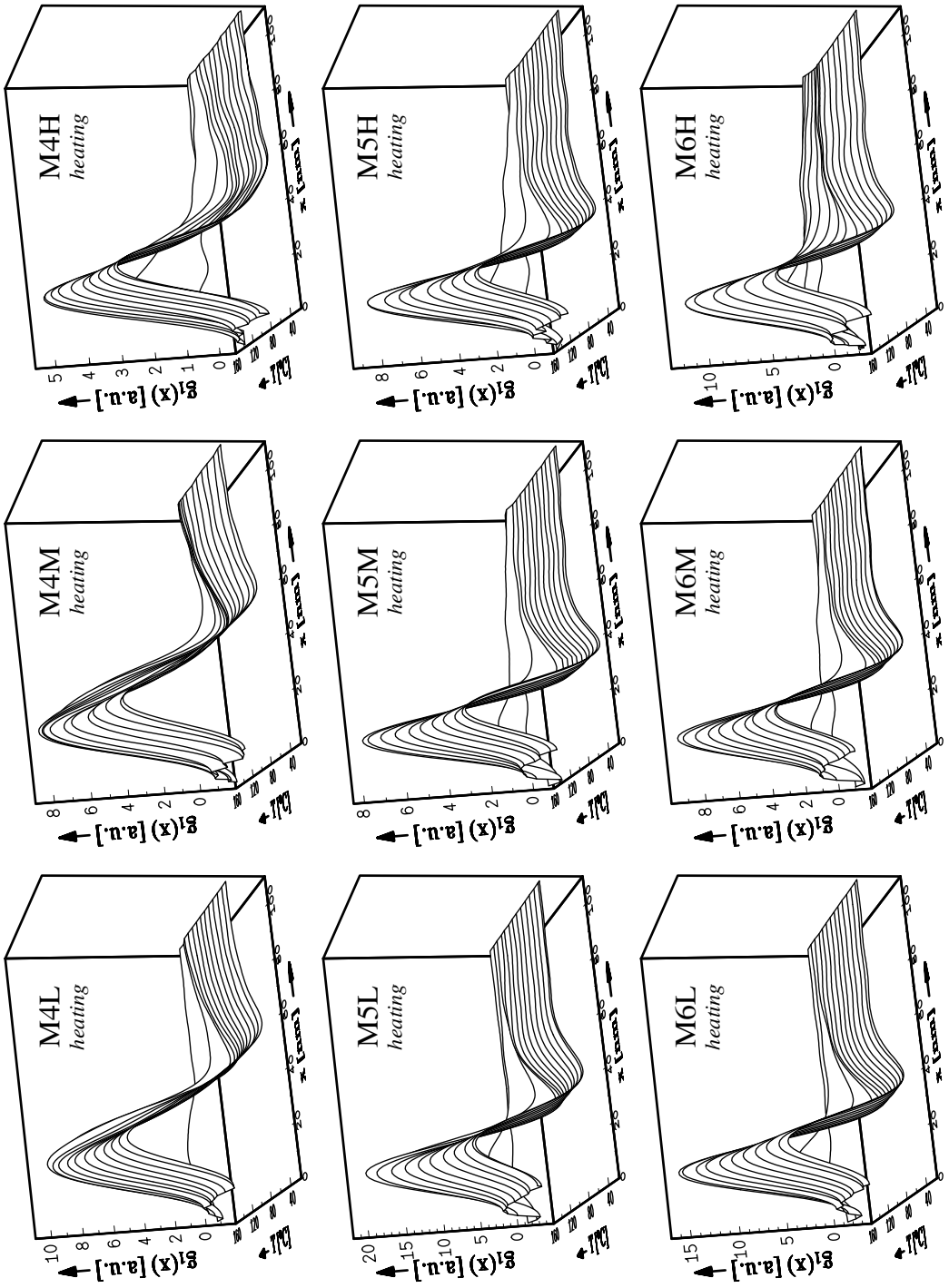

Figure 16: Interface distribution functions (IDFs) $g_1(x)$ computed from the scattering curves of UHMWPE as a function of molecular mass and molding pressure during heating and melting.

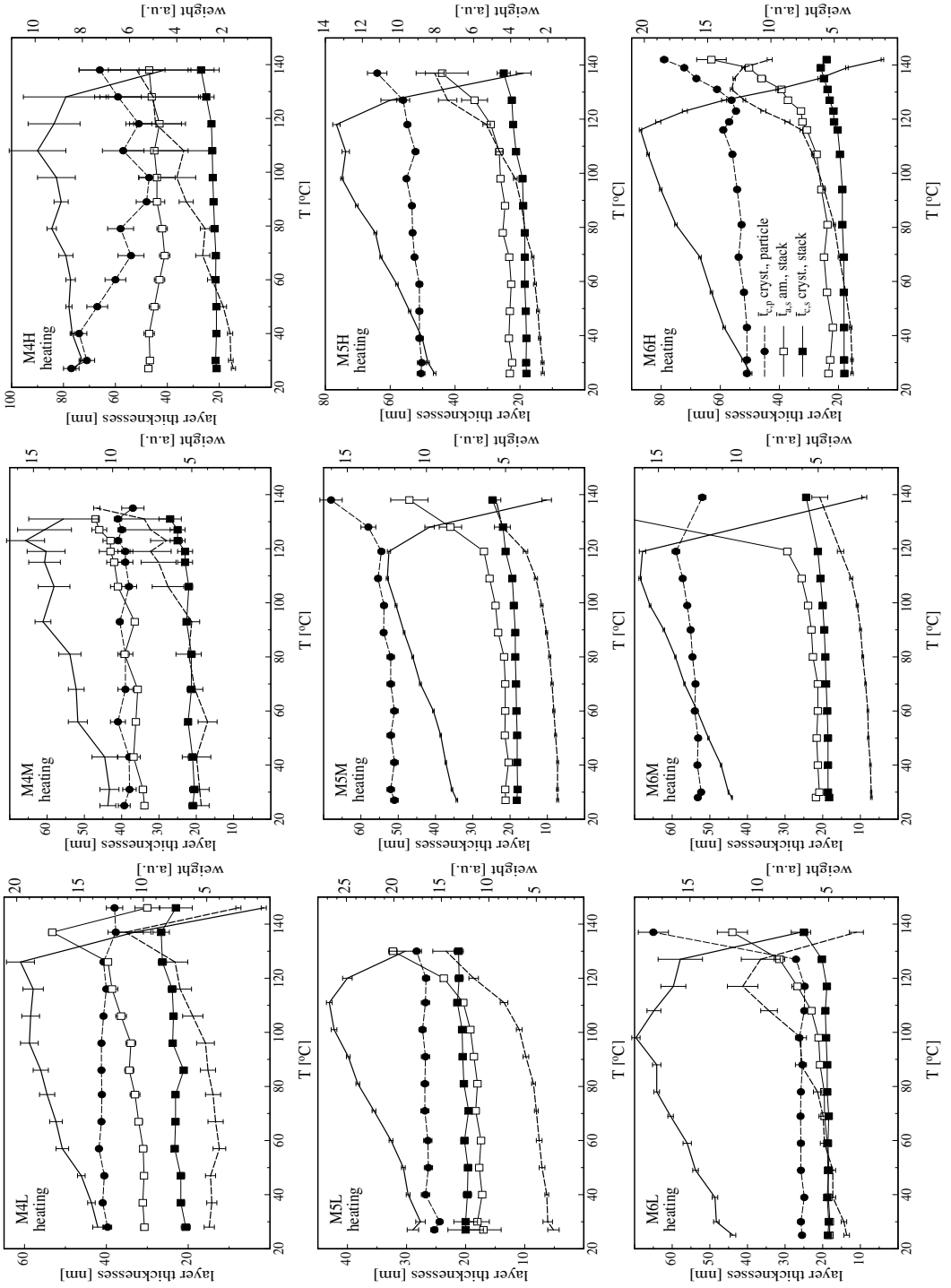

Figure 17: Nanostructure parameters from model fits of UHMWPE series during heating as determined from the IDFs. Curves without symbols show the strength of components. Curves marked by symbols show layer thicknesses. Crystalline layers carry filled symbols. Solid lines: The stacks. Broken lines: The uncorrelated lamellae.

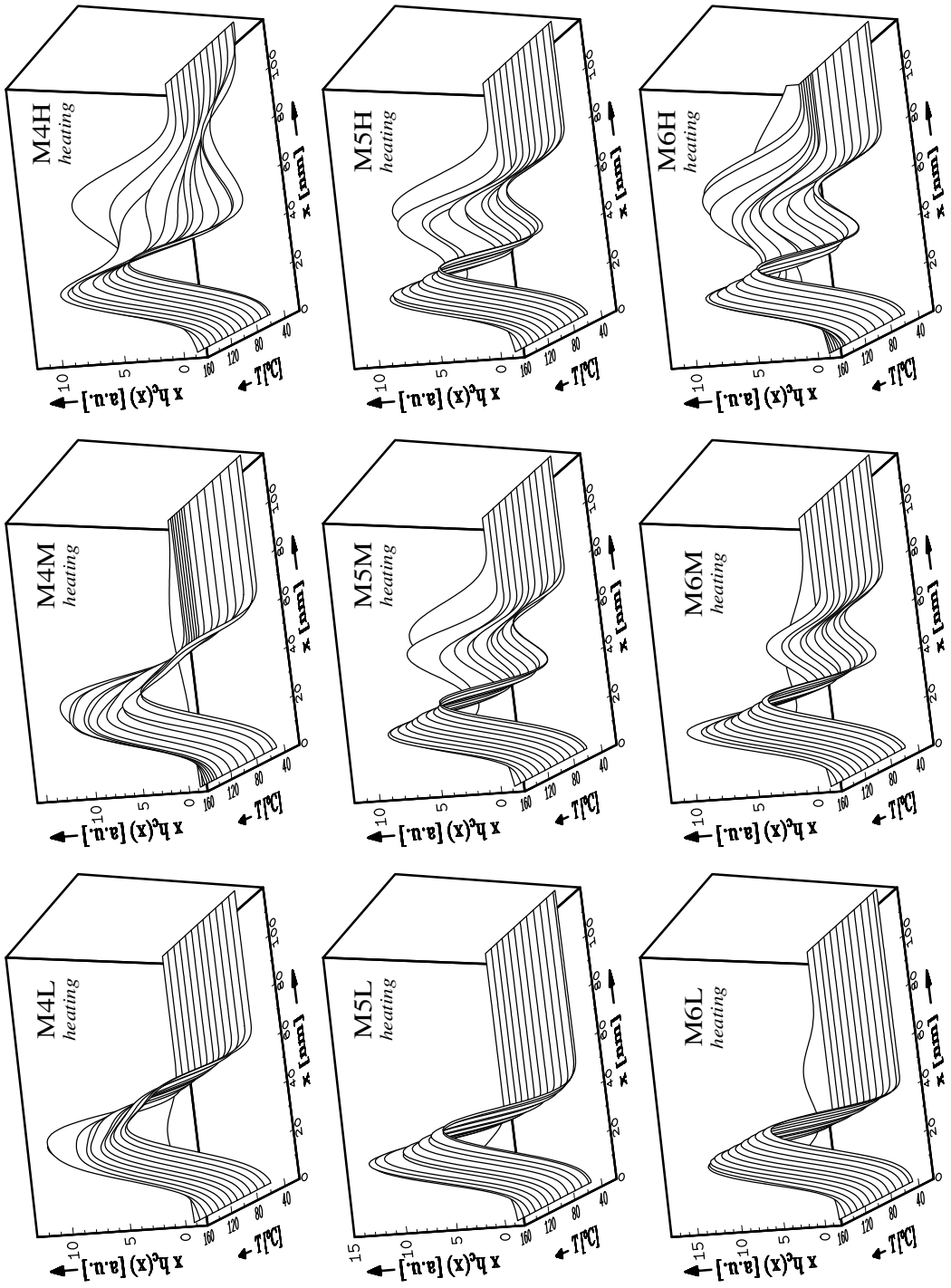

Figure 18: Crystalline volume $x\,h_c\,(x)$ as a function of lamella thickness x, temperature, molecular mass, and molding pressure during heating and melting of UHMWPE.

The samples from medium and high pressure clearly exhibit two crystalline layer thickness populations in the plots. Especially for the high pressure samples (right column) it becomes obvious that considerable amounts of "extended chain lamellae" are formed during the heating and only after the crystal lamellae from the stacks start to melt. Thus USAXS reveals two processes coupled to each other, in which the melting of conventional crystalline layers initiates formation of extended chain lamellae. The DSC experiment shows that the net external heat flow of the superimposed processes is negligible. Only the subsequent melting of the thick crystal lamellae is observed in the thermogram.

4 Conclusions

The qualitative analysis of the multi–dimensional chord distribution supplies the researcher with information on domain size, domain shape, domain orientation, range of order and last but not least on the number of components in the structure and their mutual arrangement in space. This information is valuable input for the design of an adapted structural model.

By fitting such a model to the scattering data it should become possible to separate the components of the structure and to quantitatively describe their statistics, as has been done in earlier work for 1D stacking statistics [23, 25, 56] and for 1D projections from fiber patterns [6]. If an *in–situ* experiment is monitored by recording scattering patterns, the experimental parameters like elongation, temperature or time, in conjunction with the observed structural changes, will help with the task of understanding the complexity of the morphologies which show up in multi–dimensional chord distribution functions. Moreover, the multi–dimensional relations among the components of a multi–component morphology may help to enlighten the nature of the processes governing structure formation and change in polymer materials on the nanometer scale.

Finally, there is some potential for advance of the method itself. Adjustment of the order of the derivative [73, 74] applied to the density $\rho(\mathbf{r})$ for image construction may be used to switch to a different contrast. The autocorrelation of the second derivatives of the density, for example, could be used to tag the widths of the transition zones between the phases. And it should be mentioned that the method, in principle, permits to change the order of the derivative continuously and gradually. Thus the effect of such fine–tuning to the clarity of interesting nanostructural features in a modified CDF might be studied, favorably in combination with electron microscopic studies and evaluations of synthetic model scattering patterns.

Acknowledgments. This study has been carried out in the frame of the HASYLAB project II–98–067, *"Polymers with Fiber Symmetry"* and in the frame of project RUM–047–97, *"Novel Block–Copolymers with Improved Service Properties"*. Funding by the German and the Rumanian Ministries for Education and Research is gratefully acknowledged.

References

1. Riekel, C. Bösecke, P. Sánchez del Rio, M.; *Rev. Sci. Instrum.* **1992**; *63*, 974.
2. Elleaume, P.; *Rev. Sci. Instrum.* **1992**; *63*, 321.
3. Bonart, R.; *Kolloid Z. u. Z. Polymere* **1966**; *211*, 14.
4. Stribeck, N.; *J. Polym. Sci., Part B: Polym. Phys.* **1999**; *37*, 975.
5. Stribeck, N. Fakirov, S. Sapoundjieva, D.; *Macromolecules* **1999**; *32*, 3368.
6. Stribeck, N.; *ACS Symp. Ser.* **2000**; *739*, 41.
7. Cohen, Y. Thomas, E. L.; *J. Polym. Sci., Part B: Polym. Phys.* **1987**; *B25*, 1607.
8. Hall, I. H. Mahmoud, E. A. Carr, P. D. Geng, Y. D.; *Colloid Polym. Sci.* **1987**; *265*, 383.
9. Hall, I. H. Hussain, B. H.; *Colloid Polym. Sci.* **1990**; *268*, 12.
10. Kumar, S. Warner, S. Grubb, D. T. Adams, W. W.; *Polymer* **1994**; *35*, 5408.
11. Ruland, W.; *J. Appl. Cryst.* **1971**; *4*, 70.

12. Wolff, T. Burger, C. Ruland, W.; *Macromolecules* **1994**; *27*, 3301.

13. Ruland, W.; *Macromolecules* **1987**; *20*, 87.

14. Siemann, U. Ruland, W.; *Colloid Polym Sci* **1982**; *260*, 999.

15. Ciccariello, S.; *Acta Cryst.* **1985**; *A41*, 560.

16. Ciccariello, S. Benedetti, A.; *J. Appl. Cryst.* **1986**; *19*, 195.

17. Stribeck, N. Ghioca, P. Buzdugan, E.; *J. Appl. Cryst.* **1997**; *30*, 708.

18. Porod, G.; *Kolloid-Z.* **1951**; *124*, 83.

19. Murthy, N. S. Zero, K. Grubb, D. T.; *Polymer* **1997**; *38*, 1021.

20. Murthy, N. S. Grubb, D. T. Zero, K.; *ACS Symp. Ser.* **2000**; *739*, 24.

21. Stribeck, N.; *J. Appl. Cryst.* **2001**; *34*, 496.

22. Stribeck, N.; *Colloid Polym. Sci.* **2001**; *in print*.

23. Flores, A. Pietkiewicz, D. Stribeck, N. Roslaniec, Z. Baltà Calleja, F. J.; *Macromolecules* **2001**; *34*, 8094.

24. Stribeck, N. Fakirov, S.; *Macromolecules* **2001**; *34*, 7758.

25. Wang, Z. Hsiao, B. S. Stribeck, N. Gehrke, R.; *Macromolecules* **2001**; *accepted*.

26. Stribeck, N. Buzdugan, E. Serban, S. Gehrke, R.; *Macromol. Chem. Phys.* **2001**; *in print*.

27. Buhmann, M. D.; *Acta Numerica* **2000**; *9*, 1.

28. Stribeck, N.; *Colloid Polym. Sci.* **1992**; *270*, 9.

29. *pv–wave Version 6.10*; pv—-wave Version 6.10 (1997), Visual Numerics Inc., Boulder, Colorado.

30. Vonk, C. G.; *Colloid Polym. Sci.* **1979**; *257*, 1021.

31. Méring, J. Tchoubar, D.; *J. Appl. Cryst.* **1968**; *1*, 153.

32. Ruland, W.; *Colloid Polym. Sci.* **1977**; *255*, 417.

33. Stribeck, N. Ruland, W.; *J. Appl. Cryst.* **1978**; *11*, 535.

34. Press, W. H. Teukolsky, S. A. Vetterling, W. T. Flannery, B. B.; *Numerical Recipes in C*; Cambridge: Cambridge University Press; **1992**.

35. Guinier, A. Fournet, G.; *Small–Angle Scattering of X–Rays*; London: Chapman and Hall; **1955**.

36. Glatter, O. Kratky, O., eds.; *Small Angle X–ray Scattering*; London: Academic Press; **1982**.

37. Feigin, L. A. Svergun, D. I.; *Structure Analysis by Small–Angle X–Ray and Neutron Scattering*; New York: Plenum Press; **1987**.

38. Baltà Calleja, F. J. Vonk, C. G.; *X–Ray Scattering of Synthetic Polymers*; Amsterdam: Elsevier; **1989**.

39. Fischer, L. Haschberger, R. Ziegeldorf, A. Ruland, W.; *Colloid Polym. Sci.* **1982**; *260*, 174.

40. Fiedel, H. W. Wenig, W.; *Colloid Polym. Sci.* **1989**; *267*, 369.

41. Santa Cruz, C. Stribeck, N. Zachmann, H. G. Baltà Calleja, F. J.; *Macromolecules* **1991**; *24*, 5980.

42. Stribeck, N. Zachmann, H. G. Bayer, R. K. Baltà Calleja, F. J.; *J. Mater. Sci.* **1997**; *32*, 1639.

43. Stribeck, N. Sapoundjieva, D. Denchev, Z. Apostolov, A. A. Zachmann, H. G. Stamm, M. Fakirov, S.; *Macromolecules* **1997**; *30*, 1329.
44. Schmidtke, J. Strobl, G. Thurn-Albrecht, T.; *Macromolecules* **1997**; *30*, 5804.
45. Stribeck, N. Reimers, C. Ghioca, P. Buzdugan, E.; *J. Polym. Sci., Part B: Polym. Phys.* **1998**; *36*, 1423.
46. Chen, H.-L. Li, L.-J. Lin, T.-L.; *Macromolecules* **1998**; *31*, 2255.
47. Thünemann, A. F. Lochhaas, K. H.; *Langmuir* **1998**; *14*, 6220.
48. Heck, B. Hugel, T. Iijima, M. Sadiku, E. Strobl, G.; *New J. Phys.* **1999**; *1*, 17.1.
49. Thünemann, A. F. Ruland, W.; *Macromolecules* **2000**; *33*, 2626.
50. Iijima, M. Strobl, G.; *Macromolecules* **2000**; *33*, 5204.
51. Wutz, C. Stribeck, N. Gieseler, D.; *Coll. Polym. Sci.* **2000**; *278*, 1061.
52. Heck, B. Hugel, T. Iijima, M. Strobl, G.; *Polymer* **2000**; *41*, 8839.
53. Fu, Q. Heck, B. Strobl, G. Thomann, Y.; *Macromolecules* **2001**; *34*, 2502.
54. Hsiao, B. S. Verma, R. K.; *J. Synchrotron Radiat.* **1998**; *5*, 23.
55. Kolb, R. Wutz, C. Stribeck, N. v. Krosigk, G. Riekel, C.; *Polymer* **2001**; *42*, 5257.
56. Stribeck, N.; *Colloid Polym. Sci.* **1993**; *271*, 1007.
57. Stribeck, N. Polizzi, S. Bösecke, P. Zachmann, H. G.; *Rev. Roumaine Chem.* **1989**; *34*, 635.
58. Stribeck, N. Bösecke, P. Polizzi, S.; *Colloid Polym. Sci.* **1989**; *267*, 687.
59. Stribeck, N. Bayer, R. von Krosigk, G. Gehrke, R.; *Polymer* **2001**; *submitted*.
60. Hugel, T. Strobl, G. Thomann, R.; *Acta Polym.* **1999**; *50*, 214.
61. Wang, J. Alvarez, M. Zhang, W. Wu, Z. Li, Y. Chu, B.; *Macromolecules* **1992**; *25*, 6943.
62. Hsiao, B. S. Gardner, K. H. Wu, D. Q. Chu, B.; *Polymer* **1993**; *34*, 3996.
63. Bassett, D. C. Olley, R. H. Al Raheil, I. A. M.; *Polymer* **1988**; *29*, 1745.
64. Wunderlich, B.; *Macromolecular Physics*; vol. 1; New York: Academic Press; **1973**.
65. Vonk, C. G. Kortleve, G.; *Kolloid-Z. u. Z. Polymere* **1967**; *220*, 19.
66. Barnes, J. D. Kolb, R. Barnes, K. Nakatani, A. I. Hammouda, B.; *J. Appl. Cryst.* **2000**; *33*, 758.
67. Yasuniwa, M. Yamaguchi, M. Nakamura, A. Tsubakihara, S.; *Polym. J.* **1990**; *22*, 411.
68. Baltá Calleja, F. J. Öhm, O. Bayer, R. K.; *Polymer* **1994**; *35*, 4775.
69. Hikosaka, M. Amano, R. Rastogi, S. Keller, A.; *Macromolecules* **1997**; *30*, 2067.
70. Liangbin, L. Pong, L. Rui, H. Wuyi, F. Yunwei, L. Hai, H.; *J. Mater. Sci. Lett.* **1999**; *18*, 609.
71. Flores, A. Baltá Calleja, F. J. Bassett, D. C.; *J. Polym. Sci., Part B: Polym. Phys.* **1999**; *37*, 3151.
72. Shcherbina, M. A. Chvalun, S. N. Aulov, V. A. Selikhova, V. I. Bakeev, N. F.; *Polymer science. Series A.* **2001**; *43*, 72.
73. Burger, C. Ruland, W.; *Acta Cryst.* **2001**; *A57*, 482.
74. Ciccariello, S.; *J. Math. Phys.* **1995**; *36*, 219.